Optical spectra and exciton-light coupled modes of a spherical semiconductor nanocrystal

Hiroshi Ajiki, Tetsuya Tsuji, Kiyohiko Kawano, and Kikuo Cho
Department of Physical Science, Graduate School of Engineering Science, Osaka University, Toyonaka, Osaka 560-8531, Japan
(Received 28 April 2002; published 31 December 2002)

The structures of optical spectra of a semiconducting sphere are studied over a wide range of radius. The calculation is based on a ''microscopic nonlocal theory'' and we reformulate the theory to simplify the procedure. The nonlocal theory enables us to analyze correspondences between spectral peaks and exciton states directly, decompose a scattered field into an exciton contribution and the Mie scattering, and provide complex eigenenergies of the exciton-light coupled modes. The imaginary part of the eigenenergy gives the radiative decay width of the mode, and for each mode there exists an optimal radius to enhance the width. When the Mie scattering becomes comparable to the scattering by exciton, there appears a dip structure in the optical spectra around the energy of the exciton-light coupled mode.

DOI: 10.1103/PhysRevB.66.245322 PACS number(s): 71.36.+c, 78.67.Hc

I. INTRODUCTION

Recent progress in fabrication techniques makes it possible to design both material excitations and radiation field. Through the microscopic designing of materials, one can control the energy level scheme and the corresponding wave functions of the excited states. At the same time, the radiation field in the matter acquires different spatial structure, a typical case of which is the formation of cavity modes due to the arrangement of materials. These aspects lead us to expect the controllability of radiation-matter interaction at a microscopic level. Thus the interaction of light with the excitations in various nanostructures, particularly excitons in semiconductors, has attracted considerable attention.

In order to understand the energy level scheme and the corresponding wave functions of a confined exciton, we need to consider the confining potential, the electron-hole (e-h) exchange interaction, and the effect of background polarization which leads to the bulklike screening of the Coulomb interaction and the mirror image effect due to surface charge density. These features should exist in any confined system, but it is not easy to take all of them into theoretical account for a general shape of confinement. An exception is the case of spherical confinement treated by us.[1,2] The detailed energy scheme with the assignment of longitudinal (L), transverse (T), and L-T mixed characters is now available for arbitrary size of weak confinement. With such a precise knowledge at hand, we are now able to accurately study the radiation-matter interaction for spherical confinement, such as correspondences between quantized energy levels and spectral resonances, the T and L characters of each spectral peaks, the radiative shifts and widths of the exciton levels, the interference between the Mie scattering due to the background polarization and the exciton scattering, and so on.

So far, the optical spectra of an exciton in a spherical nanocrystal were calculated according to the macroscopic scheme with the assumption of additional boundary condition (ABC) as well as the Maxwell boundary conditions.[3,4] The effect of the e-h exchange interaction is taken into account in terms of the coupling of induced polarization with depolarization field. The adopted ABC is the Pekar type, in which the exciton polarization arising from the superposition of bulk polaritons vanishes at the spherical boundary.[5] In these calculations, the size dependence of the spectral peaks was studied for small radius, where the long wavelength approximation (LWA) was valid, and they clarified a certain experimental feature. However, this method does not allow to make detailed correspondences between the calculated peaks and the exciton levels with respect to the L, T, and/or L-T mixed characters, and the radiative shifts and widths of the levels.

In order to overcome these difficulties, we can use a microscopic nonlocal response theory[6] based on the calculation of the energy level scheme mentioned above. In this framework, we determine the matter polarization and electromagnetic (EM) field self-consistently from the microscopic knowledge of the system such as the matter energy levels and the accompanying matrix elements of induced dipole density (or polarization). The scattered EM field is calculated by convoluting the radiation Green's function with the self-consistently determined polarization, which enables us to study explicitly the correspondences between the spectral peaks and the exciton states.

Since the nonlocal theory gives the exciton scattering, the method is suitable to decompose the total scattered field into the contributions of exciton (or resonant) and background (or nonresonant) polarizations. The latter of which is the well-known Mie scattering from a dielectric sphere,[7] if the nonresonant polarization is assumed to be described by a constant background susceptibility. In the total scattering cross section, these two contributions are expected to make interference between them. For a small radius sphere, the exciton scattering dominates and the Mie scattering is weak, so that the interference is not remarkable. As the radius becomes larger, the contribution of the Mie scattering gets stronger, which results in the interference with the exciton scattering.

In the original version of the nonlocal theory, we use the T component of the Maxwell Green's function. Although the extraction of the T component from the full Green's function is simple in some cases, it becomes a tedious task in many geometries with surfaces and/or interfaces including the case of a sphere. In this work, we exploit a revised form of the nonlocal theory, where the full Green's function can be used without splitting it into T and L components.

In terms of this revised scheme, we study the linear optical spectra for a wider range of size than that studied before. The spectral resonances can be precisely analyzed in terms of the complex eigenenergies $\Omega_j=\omega_j+i\omega_j'$ $(j=1,2,\ldots)$ of the exciton-light coupled modes, which are obtained from the roots of the equation $\det|\mathbf{S}|=0$, where

$$S_{\mu\nu}=(E_{\mu 0}-\hbar\omega)\delta_{\mu\nu}+\tilde{A}_{\mu 0,0\nu}(\omega). \tag{1}$$

In this expression, $E_{\mu 0}$ is the excitation energy of the matter and $\tilde{A}_{\mu 0,0\nu}(\omega)$ is the interaction energy between the two components of the induced polarization accompanying the excitations $0\rightarrow\mu$ and $0\rightarrow\nu$.

The original and revised frameworks of the nonlocal theory provide the same results. The energy terms $E_{\mu 0}\delta_{\mu\nu}+\tilde{A}_{\mu 0,0\nu}$ contain both *e-h* exchange interaction and radiative correction (the radiative shift and width). The difference between the two frameworks is the term taking care of the *e-h* exchange interaction, which is included in $\tilde{A}_{\mu 0,0\nu}$ in the new, and in $E_{\mu 0}$ in the original version. A different type of analysis of the exciton-light coupled modes was made in Ref. 3 in terms of the scattering phase, which however is restricted to the case of small radius satisfying the LWA. In contrast, the merit of the nonlocal theory is the absence of a restriction on sample size.

This paper is organized as follows. In Sec. II we reformulate the nonlocal theory. The reformulation makes the calculation much simpler in the present case. In Sec. III exciton states confined in a spherical semiconductor are briefly summarized. Including the *e-h* exchange interaction, we can classify exciton states into the *L*, *T*, and *L-T* mixed modes. The oscillator strength of each classified level is found. In Sec. IV the scattering cross section is calculated based on the reformulated nonlocal theory. We decompose the cross section into scattering by exciton, Mie scattering, and their cross term, and discuss the contribution of exciton to the total cross section. The exciton-light coupled modes are studied comprehensively by solving the secular equations in Sec. V. A summary is given in Sec. VI.

II. REFORMULATION OF NONLOCAL RESPONSE THEORY

In the study of the radiation-matter interaction, there are two approaches with respect to the choice of matter Hamiltonian and the EM field interacting with material excitation in the other part of the Hamiltonian.[8] In one case (A), one takes the matter Hamiltonian H_A with full Coulomb interaction and the transverse (*T*) components of the Maxwell field. In the other case (B), the matter Hamiltonian H_A-H_{PP}, where H_{PP} is the Coulomb interaction among the induced charge densities, and the full Maxwell field. The full Maxwell field contains the longitudinal (*L*) as well as the *T* components.

The original formulation of the nonlocal response theory[6] is made according to the scheme (A), which is also applicable to the nonlinear response.[9] The central factors determining the response are the excitation energies of matter and the radiative corrections. The latter is the interaction energy among the induced polarizations via transverse, i.e., vacuum EM field, the Green's function for which is known in a simple form. In this framework, all the transitions of the matter system can be formally included as dynamical variables. However it is usual to treat only the resonant components explicitly and to regard the nonresonant part as the background polarization to be described in terms of a constant background susceptibility.

The effect of the background polarization can be renormalized into the EM Green's function, by which one can evaluate the scattered field via the radiative shifts and widths of matter excitation energies.[10] This procedure works well in a simple case such as a slab geometry with normal incidence, where only the *T* components of EM field is relevant. However, it becomes complicated when the background polarization contains both *T* and *L* components, which makes it rather tedious to extract the *T* component of the EM Green's function to calculate the radiative correction. A simpler way to circumvent this situation is to adopt the scheme (B) mentioned above.

In the scheme (B), the interaction energy H_{PP} can be paraphrased as the interaction between matter polarization and the depolarization field due to induced polarization. Since the full EM Green's function describes the propagation of both the *L* and *T* fields, the interaction among the induced polarizations via EM field represents both the radiative correction (via the *T* field) and H_{PP} (via the *L* field). For semiconductors, H_{PP} has another interpretation, i.e., the electron-hole exchange interaction.

Thus, the two schemes (A) and (B) provide different ways to look at matter and EM field, either as a sum of H_A plus the radiative correction via *T* modes EM field, or as a sum of H_A-H_{PP} plus the interaction among the induced polarizations via full Maxwell field (with *T* and *L* components). Their equivalence can be explicitly shown only for linear response,[8] but it is enough for the present purpose.

In the electric dipole representation, the interaction of exciton and EM field is written as

$$H_{\rm int}=-\int d\mathbf{r}\hat{\mathbf{P}}(\mathbf{r})\cdot\mathbf{E}(\mathbf{r}), \tag{2}$$

where $\hat{\mathbf{P}}$ is the polarization operator of the matter and $\mathbf{E}$ is the Maxwell electric field including both *T* and *L* components.

In the linear response theory, the induced exciton polarization is given by

$$\mathbf{P}_{\rm ex}(\mathbf{r},\omega)=\int d\mathbf{r}'\boldsymbol{\chi}(\mathbf{r},\mathbf{r}';\omega)\cdot\mathbf{E}(\mathbf{r}'), \tag{3}$$

where $\boldsymbol{\chi}(\mathbf{r},\mathbf{r}';\omega)$ is the susceptibility tensor

$$\boldsymbol{\chi}(\mathbf{r},\mathbf{r}')=\sum_{\xi}\frac{\langle 0|\hat{\mathbf{P}}(\mathbf{r})|\xi\rangle\langle\xi|\hat{\mathbf{P}}(\mathbf{r}')|0\rangle}{E_{\xi}-\hbar\omega-i\gamma}, \tag{4}$$

with γ being a phenomenological damping constant. The $|0\rangle$ denotes the ground state of electron system, and $|\xi\rangle$ represents the exciton states obtained without the *e-h* exchange

interaction. The non-resonant term of the susceptibility is assumed to be described by the background dielectric constant inside a sample.

From the Maxwell equations we get

$$\nabla\times\nabla\times\mathbf{E}(\mathbf{r})-q^2\epsilon_{\rm bg}(\mathbf{r})\mathbf{E}(\mathbf{r})=4\pi q^2\mathbf{P}_{\rm ex}(\mathbf{r}), \tag{5}$$

where $\epsilon_{\rm bg}$ is the background dielectric constant and $q=\omega/c$. The solution of this equation is given by

$$\mathbf{E}(\mathbf{r})=\mathbf{E}_0(\mathbf{r})+\int d\mathbf{r}'\,\mathbf{G}(\mathbf{r},\mathbf{r}')\cdot\mathbf{P}_{\rm ex}(\mathbf{r}'), \tag{6}$$

where $\mathbf{E}_0$ is the solution of Eq. (5) for $\mathbf{P}_{\rm ex}(\mathbf{r})=0$, and the dyadic Green's function $\mathbf{G}(\mathbf{r},\mathbf{r}')$ satisfies the equation

$$\nabla\times\nabla\times\mathbf{G}(\mathbf{r},\mathbf{r}')-q^2\epsilon_{\rm bg}(\mathbf{r})\mathbf{G}(\mathbf{r},\mathbf{r}')=4\pi q^2\mathbf{I}\delta(\mathbf{r}-\mathbf{r}'), \tag{7}$$

with $\mathbf{I}$ being the identity tensor. The Green's functions of simple inhomogeneous media such as single or multilayer structures of slabs, cylinders, and spheres, are given in Ref. 11. The field $\mathbf{E}_0$ can be written as the sum of an incident field $\mathbf{E}_i$ and the field $\mathbf{E}_{\rm bg}$ scattered by the background dielectric $\epsilon_{\rm bg}(\mathbf{r})$.

Combining Eqs. (3) and (6), we have a self-consistent equation for the total field $\mathbf{E}$ as follows:

$$\mathbf{E}(\mathbf{r})=\mathbf{E}_i+\mathbf{E}_{\rm bg}+\int d\mathbf{r}'\int d\mathbf{r}''\mathbf{G}(\mathbf{r},\mathbf{r}')\cdot\boldsymbol{\chi}(\mathbf{r}',\mathbf{r}'')\cdot\mathbf{E}(\mathbf{r}'') \tag{8}$$

The inner products of Eq. (8) with $\langle\xi|\hat{\mathbf{P}}(\mathbf{r})|0\rangle$ integrated over $\mathbf{r}$ lead to the linear algebraic equations for the new variables F_ξ as

$$(E_\xi-\hbar\omega-i\gamma)F_\xi+\sum_{\xi'}\tilde{A}_{\xi\xi'}F_{\xi'}=F_\xi^{(0)}, \tag{9}$$

with

$$F_\xi=\frac{1}{E_\xi-\hbar\omega-i\gamma}\int d\mathbf{r}\langle\xi|\hat{\mathbf{P}}(\mathbf{r})|0\rangle\cdot\mathbf{E}(\mathbf{r}), \tag{10}$$

$$F_\xi^{(0)}=\int d\mathbf{r}\langle\xi|\hat{\mathbf{P}}(\mathbf{r})|0\rangle\cdot[\mathbf{E}_i(\mathbf{r})+\mathbf{E}_{\rm bg}(\mathbf{r})], \tag{11}$$

$$\tilde{A}_{\xi\xi'}=-\int d\mathbf{r}\int d\mathbf{r}'\langle\xi|\hat{\mathbf{P}}(\mathbf{r})|0\rangle\cdot\mathbf{G}(\mathbf{r},\mathbf{r}')\cdot\langle0|\hat{\mathbf{P}}(\mathbf{r}')|\xi'\rangle, \tag{12}$$

where Eq. (4) is used.

The factor $\tilde{A}_{\xi\xi'}$ represents the interaction between the induced polarizations $\langle0|\hat{\mathbf{P}}(\mathbf{r})|\xi\rangle$ and $\langle0|\hat{\mathbf{P}}(\mathbf{r})|\xi'\rangle$ via the EM field, which contains both radiative correction and the *e-h* exchange interaction. The *e-h* exchange interaction, which is excluded from E_ξ, enters in $\tilde{A}_{\xi\xi'}$ via the longitudinal part of the Green's function in Eq. (12). The interaction via transverse EM field contributes to the radiative correction, i.e., radiative shift and width of each spectral peak.

Using the solution F_ξ of Eq. (9), the scattered field by exciton $\mathbf{E}_{\rm ex}$ is obtained from

$$\mathbf{E}_{\rm ex}(\mathbf{r})=\sum_\xi F_\xi\int d\mathbf{r}'\,\mathbf{G}(\mathbf{r},\mathbf{r}')\cdot\langle\xi|\hat{\mathbf{P}}(\mathbf{r}')|0\rangle. \tag{13}$$

For the case of three-dimensional confinement, the scattering cross section σ is given by

$$\sigma=\lim_{r\to\infty}\int r^2d\Omega\,\frac{|\mathbf{E}_{\rm bg}(\mathbf{r})+\mathbf{E}_{\rm ex}(\mathbf{r})|^2}{|\mathbf{E}_i(\mathbf{r})|^2}, \tag{14}$$

where Ω is the solid angle.

III. EXCITON STATES

We consider the exciton states confined in a spherical semiconductor with radius a in the weak confinement regime. We give the background dielectric constants

$$\epsilon_{\rm bg}(\mathbf{r})=\begin{cases}\epsilon_1 & \text{for } |\mathbf{r}|<a,\\ \epsilon_2 & \text{for } |\mathbf{r}|>a.\end{cases} \tag{15}$$

The difference of the background dielectric constants leads to the interface (surface) charge density which acts as the image potential in the *e-h* Coulomb and exchange interactions. In the weak confinement regime, the relative motion of exciton is approximated by that in a bulk crystal. The image potential affects the *e-h* Coulomb attraction term in the region from the interface to the depth of the effective Bohr radius.[12] This leads to the distortion of the exciton relative motion near the surface, which is reflected on the form of the ABC to be used.[12] For the excitons in CuCl to be considered later for numerical calculation, this effect is safely neglected. However, the image potential on the *e-h* exchange term provides comparable matrix elements to the bulk case because the *e-h* exchange interaction has long-range character even in the weak confinement regime as shown in Eq. (19).

The *e-h* exchange interaction can be rewritten as the dipole-dipole interaction of exciton polarizations[13–15] or as the Coulomb interaction between induced charge densities.[8] It is the part of Eq. (12) which contains the L-component of EM Green's function. Its explicit form appears later, i.e., Eq. (19). It gives the polarization-dependent energy of the longitudinal (L), transverse (T), and/or L-T mixed modes.

For the description of the induced polarization, we choose the following bases as eigenfunctions of the confined center-of-mass (c.m.) motion, which are given by[1,2]

$$\mathbf{Q}_{nJlM}(\mathbf{r})=\sqrt{\frac{2}{a^3}}\frac{j_l(k_{nl}r)}{j_{l+1}(\kappa_{nl})}\mathbf{Y}_{JlM}(\Omega), \tag{16}$$

where $j_l(x)$ is the spherical Bessel function of order l and $\kappa_{nl}=k_{nl}a$ is the nth zero of $j_l(x)$. The bases satisfy the boundary condition that the amplitude becomes zero at the spherical boundary. The induced polarization associated with this basis is given by $\mathbf{P}_\xi=\mu\mathbf{Q}_\xi$, where $\xi=(n,J,l,M)$. The intensity μ of the polarization relates to the longitudinal and transverse splitting energy Δ_{LT} of a bulk exciton as $\mu^2=\epsilon_1\Delta_{LT}/4\pi$.

The functions $\mathbf{Y}_{JlM}$ are the vector spherical harmonics.[16] They are the eigenfunctions of the sum of the angular mo-

menta $\mathbf{l}$ and $\mathbf{l}'$ ($|\mathbf{l}'|=1$), the latter of which ($\mathbf{l}'$) is related with the unit polarization vector. Thus the functions $\mathbf{Y}_{JlM}$ are written as

$$\mathbf{Y}_{JlM}(\Omega)=\sum_{m=-l}^{l}\sum_{s=-1}^{1}\langle lm1s|l1JM\rangle Y_{lm}(\Omega)\mathbf{e}_s, \quad (17)$$

where $\langle lm1s|l1JM\rangle$ is the Clebsch-Gordan coefficient, $Y_{lm}(\Omega)$ the spherical harmonics, and $\{\mathbf{e}_s\}$ the spherical unit vectors

$$\mathbf{e}_{\pm1}=\mp\frac{1}{\sqrt{2}}(\mathbf{e}_x\pm i\mathbf{e}_y), \quad \mathbf{e}_0=\mathbf{e}_z. \quad (18)$$

The quantum numbers J and M are the total angular momentum and its projection, respectively. For $J\geqslant 1$, l runs from $J-1$ to $J+1$ and for $J=0$ the allowed value of l is only 1.

In terms of the bases set $\mathbf{Q}_\xi$, the matrix elements of the Hamiltonian are given by

$$H_{\xi\xi'}=\frac{\hbar^2k_{nl}^2}{2M_{\rm ex}}\delta_{\xi\xi'}+\int d\mathbf{r}\int d\mathbf{r}'[-\nabla\cdot\mathbf{P}_\xi(\mathbf{r})]^*\left[\frac{1}{\varepsilon_1}\frac{1}{|\mathbf{r}-\mathbf{r}'|}+V_{\rm im}(\mathbf{r},\mathbf{r}')\right][-\nabla\cdot\mathbf{P}_{\xi'}(\mathbf{r}')], \quad (19)$$

where $M_{\rm ex}$ is a translational mass of exciton. The first term denotes the kinetic energy of the c.m. motion, and the second term represents the *e-h* exchange interaction. The $V_{\rm im}$ in the square bracket gives the image-potential effect.

The Hamiltonian of Eq. (19) has a block-diagonal form with respect to J and M because of the spherical symmetry. The resulting exciton energy is independent of the projection M, i.e., each level has $(2M+1)$-fold degeneracy. The exciton states are classified into the T, L, and L-T mixed modes.[1,2] The exciton states with $J=l\geqslant 1$ are the T modes whose energies are $\hbar^2k_{nJ}^2/2M_{\rm ex}$ while the states with $(J=0,l=1)$ are the L modes with energies $\hbar^2k_{n1}^2/2M_{\rm ex}+\Delta_{LT}$. All the other states constituted from $\{l=J\pm1\}$ subspace belong to the L-T mixed modes whose energies are obtained from the numerical diagonalization of Eq. (19).

Figure 1 shows the energy levels of exciton as a function of radius. Solid lines represent the L-T mixed modes with $J=1$. Dotted and dashed lines correspond to the T and L modes, respectively. The relative dielectric constant $\epsilon_1/\epsilon_2=5.6$ corresponds to the situation that exciton is confined in a spherical CuCl crystal and its surrounding is vacuum. The parameters for CuCl are chosen as $\Delta_{LT}=5.7$ meV and $M_{\rm ex}=2.3m_{\rm e}$ with $m_{\rm e}$ being the electron mass. With increasing the radius, the L-T mixed modes approach L or T modes, which was confirmed by calculating the divergence and rotation of polarization of each level.[1,2]

Oscillator strengths calculated from a formula in Ref. 2 are also indicated by solid circles whose sizes are proportional to the oscillator strengths. Although the lowest level has the largest oscillator strength for small radius, the oscillator strengths are concentrated at the levels around a specific

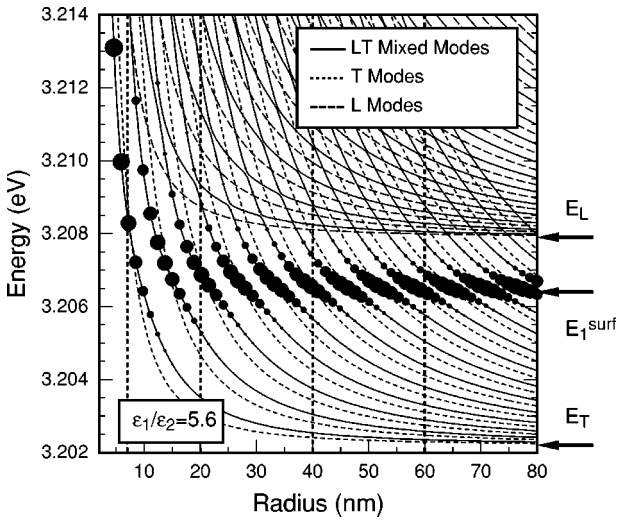

FIG. 1. Energy levels (lines) and oscillator strengths (solid circles) of exciton confined in a spherical CuCl nanocrystal as a function of radius. Solid, dotted, and dashed lines represent the L-T mixed ($J=1$), T ($J=l=1$), and L ($J=0,l=1$) modes, respectively. The oscillator strengths per volume are proportional to the size of closed circles. The vertical dotted lines denote the sizes where scattering cross sections are calculated in Fig. 2. The energies of L, T, and the surface modes in the infinite-mass limit, are indicated by E_L, $E_T(=E_0)$, and $E_1^{\rm surf}$, respectively.

energy for large sphere. The specific energy coincides with that of the surface mode in the infinite mass limit, which is given by

$$E_J^{\rm surf}=E_0+\frac{J}{J+(J+1)(\epsilon_2/\epsilon_1)}\Delta_{LT}. \quad (20)$$

This feature was first reported by Ekimov *et al.*, using the phase analysis of scattered fields.[3] It is noted that the oscillator strength becomes zero for the T-mode and L-mode states.[1,2]

IV. SCATTERING CROSS SECTION

From Eq. (14) it is seen that the total scattering cross section consists of the exciton contribution $\sigma_{\rm ex}$, Mie scattering $\sigma_{\rm Mie}$, and their cross term $\sigma_{\text{ex-}Mie}$. They are defined as

$$\sigma_{\rm ex}=\lim_{r\to\infty}\int r^2d\Omega\frac{|\mathbf{E}_{\rm ex}(\mathbf{r})|^2}{|\mathbf{E}_i(\mathbf{r})|^2}, \quad (21)$$

$$\sigma_{\rm Mie}=\lim_{r\to\infty}\int r^2d\Omega\frac{|\mathbf{E}_{\rm bg}(\mathbf{r})|^2}{|\mathbf{E}_i(\mathbf{r})|^2}, \quad (22)$$

$$\sigma_{\text{ex-}Mie}=\lim_{r\to\infty}\int r^2d\Omega\frac{2{\rm Re}[\mathbf{E}_{\rm ex}(\mathbf{r})\mathbf{E}_{\rm bg}^*(\mathbf{r})]}{|\mathbf{E}_i(\mathbf{r})|^2}. \quad (23)$$

Since $\sigma_{\rm Mie}$ is given in some textbooks (for example, see Ref. 17), we derive the expressions of $\sigma_{\rm ex}$ and $\sigma_{\text{ex-}Mie}$, and show numerical results of the present method.

A. Expressions of σ_{ex} and $\sigma_{ex\text{-}Mie}$

Let us consider elastic light scattering by exciton using the reformulated nonlocal theory. Since the exciton polarization exists in the sphere, the required Green's function satisfying Eq. (7) with the background dielectric constant Eq. (15), is given by

$$\mathbf{G}(\mathbf{r},\mathbf{r}')=\frac{4\pi i}{\epsilon_1}k_1^3\sum_{l=1}^{\infty}\frac{1}{l(l+1)}[\mathbf{m}_l(\mathbf{r},\mathbf{r}')+\mathbf{n}_l(\mathbf{r},\mathbf{r}')] - \frac{4\pi}{\epsilon_1}\hat{\mathbf{r}}\hat{\mathbf{r}}'\delta(\mathbf{r}-\mathbf{r}'), \tag{24}$$

where $\hat{\mathbf{r}}$ is the unit vector in the radial direction.[11]

In the Green's function, $\mathbf{m}_l(\mathbf{r},\mathbf{r}')$ provides the TE mode of EM field, while $\mathbf{n}_l(\mathbf{r},\mathbf{r}')$ and the last term relate to the TM mode. The $\mathbf{m}_l(\mathbf{r},\mathbf{r}')$ and $\mathbf{n}_l(\mathbf{r},\mathbf{r}')$ are given by

$$\mathbf{m}_l(\mathbf{r},\mathbf{r}')=(\nabla\times\mathbf{r})(\nabla'\times\mathbf{r}')F_l^{\mathrm{TE}}(\mathbf{r},\mathbf{r}')A_l(\Omega,\Omega'), \tag{25}$$

$$\mathbf{n}_l(\mathbf{r},\mathbf{r}')=\frac{1}{k_i^2}(\nabla\times\nabla\times\mathbf{r})(\nabla'\times\nabla'\times\mathbf{r}') \times F_l^{\mathrm{TM}}(\mathbf{r},\mathbf{r}')A_l(\Omega,\Omega'), \tag{26}$$

where k_i $(i=1,2)$ is the wave number for inside (k_1) or outside (k_2) of the sphere. If $\mathbf{r}$ appears inside (outside) of the sphere, the wave number k_i indicates k_1 (k_2). The functions $A_l(\Omega,\Omega')$ and $F_l^{\mathrm{TE(TM)}}(\mathbf{r},\mathbf{r}')$ are defined as

$$A_l(\Omega,\Omega')=\sum_{m=-l}^{l}Y_l^m(\Omega)Y_l^m{}^*(\Omega'), \tag{27}$$

$$F_l^{\mathrm{TE(TM)}}(\mathbf{r},\mathbf{r}') =\begin{cases} g_l^{\mathrm{TE(TM)}}(k_1r_>)j_l(k_1r_<) & (|\mathbf{r}|,|\mathbf{r}'|<a), \\ T_{12,l}^{\mathrm{TE(TM)}}h_l^{(1)}(k_2r)j_l(k_1r') & (|\mathbf{r}|>a,|\mathbf{r}'|<a), \end{cases} \tag{28}$$

where $r_<$ is the smaller of r and r', and conversely for $r_>$. The function $g_l^{\mathrm{TE(TM)}}(x)$ is defined as

$$g_l^{\mathrm{TE(TM)}}(x)=[h_l^{(1)}(x)+R_{12,l}^{\mathrm{TE(TM)}}j_l(x)], \tag{29}$$

where $h_l^{(1)}(x)$ is the lth spherical Hankel function of the first kind. The $R_{12,l}^{\mathrm{TE(TM)}}$ and $T_{12,l}^{\mathrm{TE(TM)}}$ represent the reflection and transmission coefficients for light propagating from the inside to the outside of the sphere, respectively, and are given by

$$R_{12,l}^{\mathrm{TE}}=\frac{\sqrt{\epsilon_1}\xi_l(\kappa_2)\xi_l'(\kappa_1)-\sqrt{\epsilon_2}\xi_l'(\kappa_2)\xi_l(\kappa_1)}{\sqrt{\epsilon_2}\psi_l(\kappa_1)\xi_l'(\kappa_2)-\sqrt{\epsilon_1}\psi_l'(\kappa_1)\xi_l(\kappa_2)}, \tag{30}$$

$$R_{12,l}^{\mathrm{TM}}=\frac{\sqrt{\epsilon_2}\xi_l(\kappa_2)\xi_l'(\kappa_1)-\sqrt{\epsilon_1}\xi_l'(\kappa_2)\xi_l(\kappa_1)}{\sqrt{\epsilon_1}\psi_l(\kappa_1)\xi_l'(\kappa_2)-\sqrt{\epsilon_2}\psi_l'(\kappa_1)\xi_l(\kappa_2)}, \tag{31}$$

$$T_{12,l}^{\mathrm{TE}}=\frac{i\sqrt{\epsilon_2}}{\sqrt{\epsilon_2}\psi_l(\kappa_1)\xi_l'(\kappa_2)-\sqrt{\epsilon_1}\xi_l(\kappa_2)\psi_l'(\kappa_1)}, \tag{32}$$

$$T_{12,l}^{\mathrm{TM}}=\frac{i\epsilon_2/\sqrt{\epsilon_1}}{\sqrt{\epsilon_1}\psi_l(\kappa_1)\xi_l'(\kappa_2)-\sqrt{\epsilon_2}\xi_l(\kappa_2)\psi_l'(\kappa_1)}, \tag{33}$$

with $\psi_l(x)=xj_l(x)$, $\xi_l(x)=xh_l^{(1)}(x)$ being the Riccati-Bessel functions and $\kappa_{1,2}=k_{1,2}a$.

The vector functions in Eqs. (25) and (26) have the form of $\nabla\times[\mathbf{r}z_l(kr)Y_{lm}]$ and $\nabla\times\nabla\times[\mathbf{r}z_l(kr)Y_{lm}]$, where $z_l(kr)$ represents spherical Bessel functions $j_l(kr)$ or $h_l^{(1)}(kr)$. These vector functions can be transformed into the different forms proportional to the vector spherical harmonics $\mathbf{Y}_{JlM}$. The transformations, which are discussed in Appendix A, are useful to calculate the $\tilde{A}_{\xi\xi'}$ of Eq. (12) in the bases of Eq. (16) because of the orthonormal relation for the vector spherical harmonics.

Using the transformation we find immediately that the T-mode exciton $(J=l)$ couples with the TE mode of the EM field. On the other hand, the LT-mixed mode of exciton couples with the TM mode of the EM field. Thus we can discuss the exciton-light interaction for TE and TM modes independently. The L-mode exciton does not couple with the transverse EM field.

We denote the interaction among the exciton polarizations via EM field $\tilde{A}_{\xi\xi'}$ as $\tilde{A}_{nJlM;n'Jl'M}^{\mathrm{TE(TM)}}$ for the TE (TM) modes. The calculated results of $\tilde{A}_{\xi\xi'}$ are summarized as follows:

$$\tilde{A}_{nJJM;n'JJM}^{\mathrm{TE}}=-\Delta_{LT}[2i\kappa_1^3\alpha(nJ)\alpha(n'J)j_J(\kappa_1)g_J^{\mathrm{TE}}(\kappa_1)+\beta(nJ)\delta_{nn'}], \tag{34}$$

$$\tilde{A}_{nJ,J+1,M;n'J,J+1,M}^{\mathrm{TM}}=-\Delta_{LT}\left\{2i\kappa_1^3\frac{J}{2J+1}\alpha(n,J+1)\alpha(n',J+1)j_{J+1}(\kappa_1)g_{J+1}^{\mathrm{TM}}(\kappa_1)+\left[-(J+1)+\frac{J}{2J+1}\beta(n,J+1)\right]\delta_{nn'}\right\}, \tag{35}$$

$$\tilde{A}_{nJ,J-1,M;n'J,J-1,M}^{\mathrm{TM}}=-\Delta_{LT}\left\{2i\kappa_1^3\frac{J+1}{2J+1}\alpha(n,J-1)\alpha(n',J-1)j_{J-1}(\kappa_1)g_{J-1}^{\mathrm{TM}}(\kappa_1)+\left[-J+\frac{J+1}{2J+1}\beta(n,J-1)\right]\delta_{nn'}\right\}, \tag{36}$$

$$\tilde{A}^{\mathrm{TM}}_{nJ,J+1,M;n'J,J-1,M}=\Delta_{LT}\left\{2i\kappa_1^3\frac{\sqrt{J(J+1)}}{2J+1}\alpha(n,J+1)\alpha(n',J-1)j_{J+1}(\kappa_1)g^{\mathrm{TM}}_{J-1}(\kappa_1)+2\sqrt{J(J+1)}\right.$$
$$\left.\times\alpha(n',J-1)\frac{\kappa_{nJ+1}}{\kappa^2_{nJ+1}-\kappa^2_{n'J-1}}\right\}, \tag{37}$$

$$\tilde{A}^{\mathrm{TM}}_{nJ,J-1,M;n'J,J+1,M}=\Delta_{LT}\left\{2i\kappa_1^3\frac{\sqrt{J(J+1)}}{2J+1}\alpha(n,J-1)\alpha(n',J+1)j_{J-1}(\kappa_1)g^{\mathrm{TM}}_{J+1}(\kappa_1)-2\sqrt{J(J+1)}\right.$$
$$\left.\times\alpha(n',J+1)\frac{\kappa_{nJ-1}}{\kappa^2_{nJ-1}-\kappa^2_{n'J+1}}\right\}, \tag{38}$$

with

$$\alpha(nJ)=\frac{\kappa_{nJ}}{\kappa^2_{nJ}-\kappa_1^2}, \tag{39}$$

$$\beta(nJ)=\frac{\kappa_1^2}{\kappa^2_{nJ}-\kappa_1^2}. \tag{40}$$

In the calculation we use the formulas of integration in Appendix B.

Next, we proceed to the calculation of $F^{(0)}_{\xi}$ in Eq. (11). The electric field $\mathbf{E}_i+\mathbf{E}_{\mathrm{bg}}$ corresponds to the field inside of the dielectric sphere in the absence of the exciton, which is obtained from the Mie scattering theory.[17] If an incident field is a linear polarized plane wave with its intensity E_i, the internal field is given by

$$\mathbf{E}_i+\mathbf{E}_{\mathrm{bg}}=E_i\sum_{l=1}^{\infty}i^l\frac{2l+1}{l(l+1)}\left[T^{\mathrm{TE}}_{21,l}\mathbf{M}_{o1l}-i\sqrt{\frac{\epsilon_2}{\epsilon_1}}T^{\mathrm{TM}}_{21,l}\mathbf{N}_{e1l}\right], \tag{41}$$

with

$$\mathbf{M}_{omn}=\boldsymbol{\nabla}\times(\mathbf{r}\psi_{omn}), \tag{42}$$

$$\mathbf{N}_{emn}=\frac{1}{k_1}\boldsymbol{\nabla}\times\boldsymbol{\nabla}\times(\mathbf{r}\psi_{emn}), \tag{43}$$

$$\psi_{omn}=\sin m\phi P^m_n(\cos\theta)j_n(k_1r), \tag{44}$$

$$\psi_{emn}=\cos m\phi P^m_n(\cos\theta)j_n(k_1r), \tag{45}$$

where $P^m_n(\cos\theta)$ is the associated Legendre function, and the z axis is chosen in the direction of the incident light. The $T^{\mathrm{TE(TM)}}_{21,l}$ is the transmission coefficients of TE (TM) waves propagating from the outside to the inside of the sphere

$$T^{\mathrm{TE}}_{21,l}=\frac{i\sqrt{\epsilon_1}}{\sqrt{\epsilon_2}\psi_l(\kappa_1)\xi_l'(\kappa_2)-\sqrt{\epsilon_1}\psi_l'(\kappa_1)\xi_l(\kappa_2)}, \tag{46}$$

$$T^{\mathrm{TM}}_{21,l}=\frac{i\epsilon_1/\sqrt{\epsilon_2}}{\sqrt{\epsilon_1}\psi_l(\kappa_1)\xi_l'(\kappa_2)-\sqrt{\epsilon_2}\psi_l'(\kappa_1)\xi_l(\kappa_2)}. \tag{47}$$

In order to calculate $F^{(0)}_{\xi}$, it is useful to transform $\mathbf{M}_{omn}$ and $\mathbf{N}_{emn}$ into the vector spherical harmonics $\mathbf{Y}_{JlM}$, and the transformations are given in Appendix A. Then the analytic expressions of $F^{(0)}_{\xi}$ are summarized as follows:

$$F^{(0)\mathrm{TE}}_{nJJM}=E_i\mu\sqrt{a^3}\sqrt{2\pi}i^J\sqrt{2J+1}T^{\mathrm{TE}}_{21,J}$$
$$\times\alpha(nJ)j_J(\kappa_1)(\delta_{M,1}+\delta_{M,-1}), \tag{48}$$

$$F^{(0)\mathrm{TM}}_{nJ,J+1,M}=-E_i\mu\sqrt{a^3}\sqrt{2\pi}i^{J+1}\sqrt{J}\sqrt{\epsilon_2/\epsilon_1}T^{\mathrm{TM}}_{21,J}$$
$$\times\alpha(n,J+1)j_{J+1}(\kappa_1)(\delta_{M,1}-\delta_{M,-1}), \tag{49}$$

$$F^{(0)\mathrm{TM}}_{nJ,J-1,M}=-E_i\mu\sqrt{a^3}\sqrt{2\pi}i^{J-1}\sqrt{J+1}\sqrt{\epsilon_2/\epsilon_1}T^{\mathrm{TM}}_{21,J}$$
$$\times\alpha(n,J-1)j_{J-1}(\kappa_1)(\delta_{M,1}-\delta_{M,-1}). \tag{50}$$

If the incident field is a linearly polarized plane wave, $F^{(0)}_{\xi}$ is finite only for $M=\pm1$. Thus we may restrict ourselves to the subspace $M=1$ and -1 to get the solution F_{ξ} of Eq. (9).

The scattered TE and TM fields by exciton in Eq. (13) are calculated as

$$\mathbf{E}^{\mathrm{TE}}_{\mathrm{ex}}=\eta k_1^3\frac{\mu}{\epsilon_1}\sum_{nJ}\sum_{M=\pm1}U_{nJM}h^{(1)}_J(k_2r)\mathbf{Y}_{JJM}, \tag{51}$$

$$\mathbf{E}^{\mathrm{TM}}_{\mathrm{ex}}=\eta k_1^3\frac{\mu}{\epsilon_1}\sum_{nJ}\sum_{M=\pm1}V_{nJM}[\sqrt{J}h^{(1)}_{J+1}(k_2r)\mathbf{Y}_{J,J+1,M}$$
$$-\sqrt{J+1}h^{(1)}_{J-1}(k_2r)\mathbf{Y}_{J,J-1,M}], \tag{52}$$

with

$$\eta=4\sqrt{2}\pi i\sqrt{a^3} \tag{53}$$

and

$$U_{nJM}=T^{\mathrm{TE}}_{12,J}F^{\mathrm{TE}}_{nJJM}\alpha(nJ)j_J(\kappa_1), \tag{54}$$

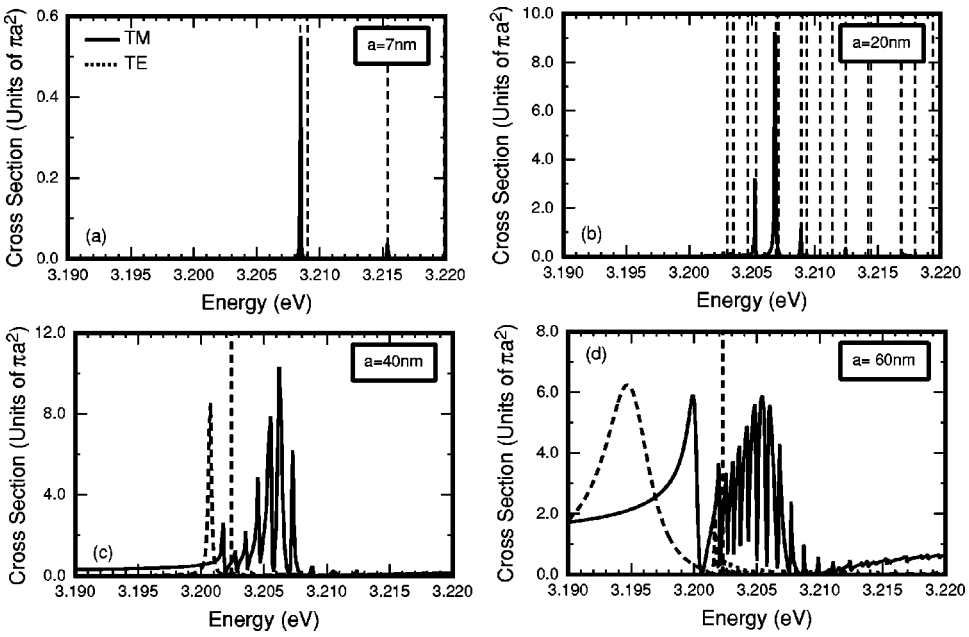

FIG. 2. Calculated total scattering cross sections of spherical CuCl nanocrystal with radii (a) 7 nm, (b) 20 nm, (c) 40 nm, and (d) 60 nm as a function of incident-light energy. The solid and dotted lines correspond to the TM and TE modes, respectively. The vertical dotted lines in (a) and (b) indicate the confined exciton levels, which are calculated including the *e-h* exchange interaction. Each vertical dotted line in (c) and (d) indicates the exciton energy at the band edge.

$$V_{nJM}=\frac{1}{2J+1}\sqrt{\frac{\epsilon_1}{\epsilon_2}}T^{\mathrm{TM}}_{12,J}[\sqrt{J}F^{\mathrm{TM}}_{nJ,J+1,M}\alpha(nJ+1)j_{J+1}(\kappa_1) - \sqrt{J+1}F^{\mathrm{TM}}_{nJ,J-1,M}\alpha(nJ-1)j_{J-1}(\kappa_1)]. \quad (55)$$

Substituting Eq. (51) or (52) into Eq. (21), we get the scattering cross section due to exciton

$$\sigma^{\mathrm{TE}}_{\mathrm{ex}}=\frac{8\pi}{E_i^2}\frac{\Delta_{LT}}{a\epsilon_2}\kappa_1^4\sum_J\sum_{M=\pm1}\sum_{nn'}U^*_{nJM}U_{n'JM}, \quad (56)$$

$$\sigma^{\mathrm{TM}}_{\mathrm{ex}}=\frac{8\pi}{E_i^2}\frac{\Delta_{LT}}{a\epsilon_2}\kappa_1^4\sum_J\sum_{M=\pm1}\sum_{nn'}(2J+1)V^*_{nJM}V_{n'JM}. \quad (57)$$

The $\sigma_{\mathrm{ex}\text{-}Mie}$ is calculated from Eqs. (51) and (52) and standard Mie scattering field $\mathbf{E}_{\mathrm{bg}}$. The transformations of Eqs. (C1) and (C2) are useful to calculate the integration with respect to the solid angle. Then we have

$$\sigma^{\mathrm{TE}}_{\mathrm{ex}\text{-}Mie}=-8\pi\kappa_1\frac{\sqrt{2\epsilon_1 a\Delta_{LT}}}{\epsilon_2 E_i} \times\sum_{nJ}\sqrt{2J+1}\mathrm{Re}[(-i)^{J+1}R^{\mathrm{TE}}_{21,J}{}^*U_{nJ1}], \quad (58)$$

$$\sigma^{\mathrm{TM}}_{\mathrm{ex}\text{-}Mie}=8\pi\kappa_1\frac{\sqrt{2\epsilon_1 a\Delta_{LT}}}{\epsilon_2 E_i} \times\sum_{nJ}(2J+1)\mathrm{Re}[(-i)^{J+1}R^{\mathrm{TM}}_{21,J}{}^*V_{nJ1}], \quad (59)$$

where the $R^{\mathrm{TE(TM)}}_{21,l}$ represents the reflection coefficients for light propagating from the outside to inside of the sphere, and given by

$$R^{\mathrm{TE}}_{21,l}=\frac{\sqrt{\epsilon_1}\psi_l'(\kappa_1)\psi_l(\kappa_2)-\sqrt{\epsilon_2}\psi_l'(\kappa_2)\psi_l(\kappa_1)}{\sqrt{\epsilon_2}\psi_l(\kappa_1)\xi_l'(\kappa_2)-\sqrt{\epsilon_1}\psi_l'(\kappa_1)\xi_l(\kappa_2)}, \quad (60)$$

$$R^{\mathrm{TM}}_{21,l}=\frac{\sqrt{\epsilon_2}\psi_l(\kappa_2)\psi_l'(\kappa_1)-\sqrt{\epsilon_1}\psi_l'(\kappa_2)\psi_l(\kappa_1)}{\sqrt{\epsilon_1}\psi_l(\kappa_1)\xi_l'(\kappa_2)-\sqrt{\epsilon_2}\psi_l'(\kappa_1)\xi_l(\kappa_2)}. \quad (61)$$

In the following, scattering spectra are calculated from Eqs. (56)–(59) and the standard Mie theory for σ_{Mie}.

B. Numerical results

We apply the present framework to an exciton confined in a spherical CuCl crystal, which is surrounded by vacuum. The energy of bulk exciton for CuCl is $E_0=3.2022$ eV at the band edge. We choose the phenomenological nonradiative damping constant $\gamma=20$ μeV, which is the best value for a thin bulk film.[18] The scattered fields $\mathbf{E}_{\mathrm{bg}}$ are evaluated by the ordinary Mie scattering theory.[17]

Figure 2 shows calculated examples of the scattering cross sections of $J=1$ component for spherical CuCl crystal with radii $a=7$, 20, 40, and 60 nm. The incident field is assumed to be a plane wave. For these small radii, the higher J components of the incident field are not scattered. The cross sections are normalized by the geometrical cross section πa^2. The solid and dotted lines correspond to the cross sections by TM and TE modes, respectively.

The vertical dotted lines in Figs. 2(a) and 2(b) denote the energy levels of the confined exciton including the *e-h* exchange interaction. For small particles with radii $a=7$ nm (a) and 20 nm (b), the scattering cross section well follows the oscillator strength. The largest scattering for $a=7$ nm comes from the lowest exciton, which is a L-T mixed mode, and has the maximum oscillator strength as shown in Fig. 1. The second lowest level has the T-mode character and does not couple with light. This is consistent with the fact that the oscillator strength is zero for T-mode exciton. For a

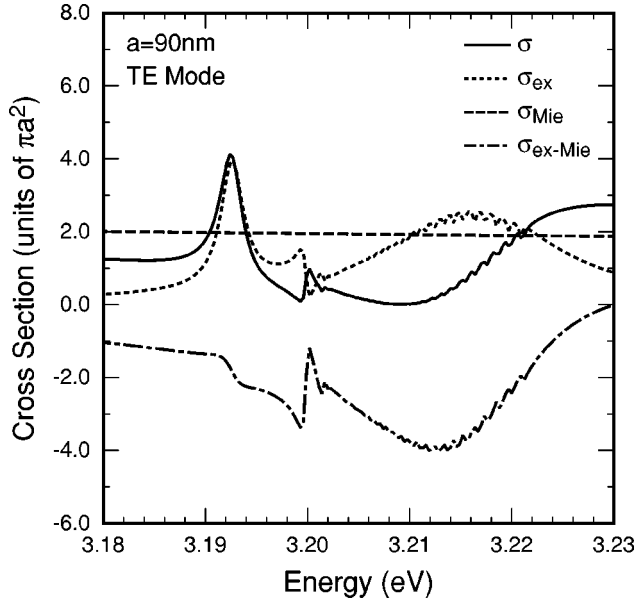

FIG. 3. A total scattering cross section (solid line) and its decomposition into exciton contribution (dotted line), Mie scattering (dashed line), and their cross terms (dashed-dotted line).

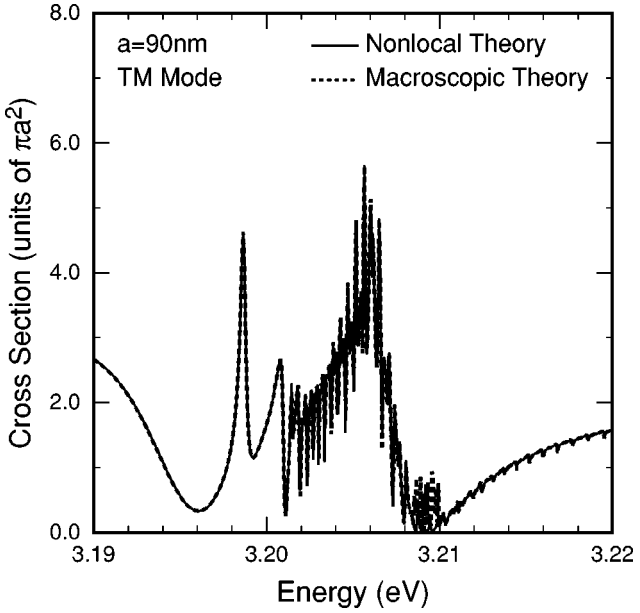

FIG. 4. Comparison between the cross section for TM modes obtained from the microscopic nonlocal theory (solid line) and the macroscopic calculation with the Pekar type ABC (dotted line).

$=20$ nm, the largest scattering occurs for the level near the surface mode in the infinite-mass limit, which is calculated as $E_1^{\mathrm{surf}}=3.2064$ eV from Eq. (20). The results are well described in terms of the oscillator strength also. The concept of the oscillator strength is meaningful if the confinement size of exciton is much smaller than the wavelength of light. The deviation of the cross section from the oscillator strength is seen for the case of radii $a=40$ and 60 nm, where the *T*-mode exciton, which has zero oscillator strength, scatters the TE-mode light significantly.

In Figs. 2 (c) and (d), energy levels of the lowest *T*-mode exciton are indicated by the vertical dotted lines, and the scattering peak due to this exciton shifts to the lower energy side, the amount of which becomes larger for $a=60$ nm than $a=40$ nm. In addition, the peak width becomes larger with increasing radius. The peak shifts and widths originate from the radiative correction, i.e., the interaction between induced polarizations via transverse EM field. The radiative correction will be discussed in the next section.

One of the advantages of using the present formulation is that the cross section can be decomposed into those due to the exciton and the background dielectric as shown in Eqs. (21)–(23). The resonance scattering σ_{ex} is dominant for small radius such as the examples in Fig. 2. However, σ_{Mie} and $\sigma_{\text{ex-}Mie}$ give significant contribution to the total cross section for larger radius.

For instance, these three contributions are depicted in Fig. 3 for the TE mode in a CuCl particle with $a=90$ nm. We choose the nonradiative damping constant γ as 0.2 meV. In the calculation we take the angular momenta up to $J=3$ because the scattering into the higher angular momenta is negligibly small for the present size. From the total scattering cross section, we extract σ_{ex} (dotted line), σ_{Mie} (dashed line), and $\sigma_{\text{ex-}Mie}$ (dashed-dotted line). Although σ_{ex} and σ_{Mie} have positive values, $\sigma_{\text{ex-}Mie}$ can take negative values. Because of the interference effect, some total scattering take dip structures near peak energies of σ_{ex}.

To study the spectral structures more precisely, let us focus on the sharp peak at 3.192 eV and the broad peak at 3.216 eV of σ_{ex}. Although the σ near 3.192 eV shows peak structure as well as the σ_{ex}, the σ near 3.216 eV exhibits dip structure that is different from the shape of the σ_{ex}. In such a large sphere, the σ_{Mie}, which is dominated by the $J=1$ component, is comparable to the σ_{ex}. Therefore the interference term $\sigma_{\text{ex-}Mie}$ gives large contribution to the $J=1$ component of the σ. Since the peak of σ_{ex} at 3.216 eV originates from the exciton states with $J=1$, the corresponding σ becomes quite different from σ_{ex} due to the term of $\sigma_{\text{ex-}Mie}$. Thus the σ exhibits the dip structure near 3.216 eV. On the other hand, the $J=2$ component of the σ is almost determined by σ_{ex}, and we have the peak structure of σ near 3.192 eV.

Before closing this section, we compare the results by two different approaches, i.e., the microscopic nonlocal theory and the macroscopic calculation using the Pekar type ABC in Fig. 4. The solid and dotted lines represent the scattering cross section of the TM modes calculated from the nonlocal theory and macroscopic calculation with the ABC, respectively. We find the two approaches to be in good agreement with each other. Slight difference around 3.209 eV comes from the insufficiency of the basis functions used for the nonlocal calculation corresponding to the quantum number *n* of $\mathbf{Q}_{nJlM}$. We also confirmed a similar agreement for the cross section for TE modes. The agreement is to be expected because the Pekar type ABC corresponds to the hard-wall boundary condition for the c.m. wave function of exciton. Thus we may use the both approaches in the calculation of scattering field. However, the nonlocal theory gives more detailed information about the *T* and *L* characters, the de-

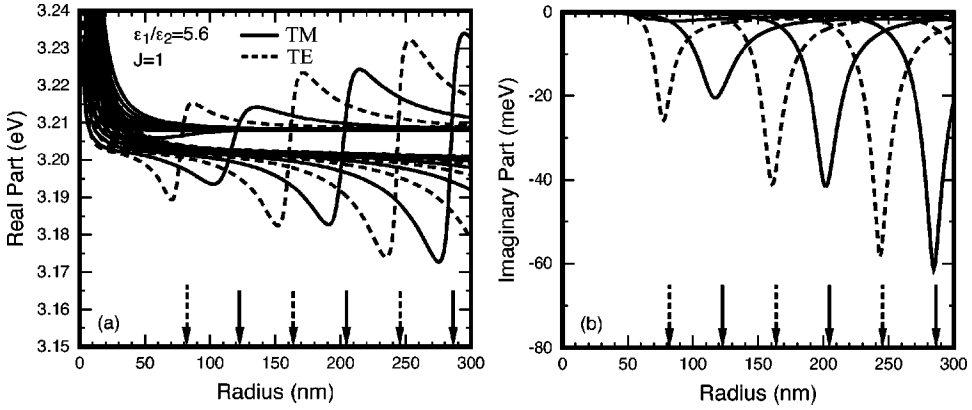

FIG. 5. Calculated real (a) and imaginary (b) parts of eigenenergy for exciton-light coupled modes with $J=1$ as a function of radius. Exciton is confined in a spherical CuCl nanocrystal. The solid and dotted lines represent the TM and TE modes, respectively. The real part gives the energy of spectral peak, and imaginary part relates to the spectral width. The solid (TM mode) and dotted (TE mode) arrows indicate the radii given by approximated conditions Eqs. (63) and (64).

composition of the exciton scattering and the Mie scattering, and the energies of the exciton-light coupled modes.

V. EXCITON-LIGHT COUPLED MODE

The spectral peaks due to exciton are characterized by the eigenenergies of the exciton-light coupled modes. The $\mathbf{E}_{\rm ex}$ is proportional to F_ξ as shown in Eq. (13), and F_ξ is the solution of Eq. (9). Thus the solutions of the secular equation

$$\det[(E_\xi-\hbar\omega)\delta_{\xi\xi'}+\tilde{A}_{\xi\xi'}(\omega)]=0, \tag{62}$$

provide the shapes of the spectral peaks, namely, the real and imaginary parts of a solution give a peak energy and a peak width. We ignore the nonradiative damping constant γ to study the radiative correction. Since the peak width originates from the coupling of exciton and light, it represents the radiative decay width. The radiative width indicates the strength of exciton-light coupling. The solution of Eq. (62) can be considered as the complex eigenenergy of the exciton-light coupled mode. In the case of bulk crystals, the exciton-light coupled mode becomes bulk polariton, and its eigenenergy is real. However, the coupled mode has lifetime in a finite crystal because of the leakage of light to the outside, and thus the eigenenergy has an imaginary part in general.

It is noted that Eq. (62) is not limited to the case of excitons, i.e., it has the same form independent of the origin of the induced polarization. This fact leads to a unified description of the dispersion equations for bulk polariton and x-ray scattering from Eq. (62).[19]

In the spherical case, the exciton-light coupled modes are classified into TE and TM modes. The TE eigenenergy is calculated by substituting Eq. (34) into Eq. (62), and the TM eigenenergy is calculated using Eqs. (35)–(38). The radiative correction $\tilde{A}_{\xi\xi'}$ is ω dependent, which becomes important for large radius. If the ω dependence can be neglected Eq. (62) is a polynomial equation of the Nth order, where N is the number of the basis functions $\{|\xi\rangle\}$. In this case, the solutions correspond to the excitons modified by the radiative shifts and widths. If, however, the ω dependence of $\tilde{A}_{\xi\xi'}$ is not negligible, Eq. (62) is no more a polynomial equation of the Nth order, and the interpretation of the solution is no more simple. The results in Fig. 5 correspond to the case of simple interpretation.

Figure 5 shows calculated results of the real (a) and the imaginary (b) parts of the eigenenergies of the exciton-light coupled modes as a function of radius. Solid and dotted lines correspond to the TM and TE modes, respectively. We again consider a spherical CuCl in vacuum. For small radius up to $\sim$50 nm, the real parts coincide with the peak energies of the exciton states including the e-h exchange interaction, and the imaginary parts (or peak widths) are almost zero. In other words, the coupling of confined exciton and light is quite small.

With increasing radius the real part of the lowest TE mode deviates from the level of exciton toward the lower energy side, and after a rapid increase it approaches the energy $E_0+\Delta_{LT}$. The corresponding imaginary part shows peak structure at the size where the real part increases rapidly. It is noted that the magnitude of this imaginary part becomes quite small for large radius. This means that the light coupling with the lowest exciton decreases with increasing the confinement size. In this region, the second lowest exciton begins to couple with light strongly. This alternating behavior of the exciton-light coupling with the increase in radius continues for higher members of the exciton states, and their maximum strengths become larger. It is found that the maximum strengths reach several tens meV. The similar behavior has also been calculated for the exciton confined in a quantum well.[20,21]

The characteristic size dependence of the radiative width can be understood roughly from the spatial patterns of the wave function of exciton and the light intensity. Around the size where the radiative width becomes maximum, the wavelengths of confined exciton and light are almost in agreement with each other. However, the sizes satisfying above condition do not coincide with the sizes giving maximum radiative widths. The crucial point is that the retarded interaction $\tilde{A}_{\xi\xi'}$

in Eqs. (34)–(38) contains the reflection coefficients $R_{12,l}^{\mathrm{TE(TM)}}$ appearing in $g_l^{\mathrm{TE(TM)}}(z)$. The $R_{12,l}^{\mathrm{TE(TM)}}$ depends on radius, and the radii giving maximum radiative widths are determined by the condition of $R_{12,l}^{\mathrm{TE(TM)}}$ being maximum, in which the denominator becomes minimum. This condition is the same as that of the Mie resonance. Using the asymptotic expansions for large argument of spherical Bessel functions, we have the radii $a_n^{\mathrm{TE(TM)}}$ which provide maximum $R_{12,l}^{\mathrm{TE(TM)}}$ as

$$a_n^{\mathrm{TE(TM)}} = \frac{n\pi}{k_1} \quad \text{for odd (even) } J, \tag{63}$$

$$a_n^{\mathrm{TE(TM)}} = \left(n + \frac{1}{2}\right)\frac{\pi}{k_1} \quad \text{for even (odd) } J, \tag{64}$$

where n is an integer. The conditions depend on only the wavelength inside of a sphere. In Fig. 5 vertical arrows indicate the radii represented by Eqs. (63) and (64). It is found that these simple expressions describe the radii with maximum radiative width quite well in the present case, though the above conditions hold better for large confinement radius. This indicates that the size enhancement of the exciton-light interaction is dominated by the cavity effect of Mie resonance. It should be noted that the enhancement condition is invalid for small ϵ_1/ϵ_2, where the cavity effect becomes small. In this case, the enhancement size would depend on the L-T splitting energy Δ_{LT} characterizing the magnitude of the exciton-light interaction.

The resonant energies and widths of the spectral peaks in Fig. 2 are in agreement with the eigenenergies of the corresponding exciton-light coupled modes. The spectral structure of σ_{ex} with 90 nm in radius (see Fig. 3) is also described by the eigenmodes, but in such large radius the total cross section is different from σ_{ex} due to the interference with the Mie scattering as shown in the previous section.

It seems that the maximum spectral or radiative widths increase monotonically toward infinity, however, the coupled mode in infinite crystals, *i.e*, bulk polariton, should have zero radiative width. Therefore it is difficult to image how the coupled mode confined in large crystal approaches bulk polariton. The missing link has been studied and reported by one of the authors in Ref. 22. The point is that the energy dependence of $\tilde{A}_{\xi\xi'}$ (the interaction between polarizations via EM field) plays an important role in spectral shapes.

VI. SUMMARY

For an exciton weakly confined in a spherical nanocrystal, we have studied the scattering cross sections and exciton-light coupled modes comprehensively by using a reformulated microscopic nonlocal theory. In our calculation, we consider the situation where the c.m. motion of the exciton is confined in an infinite hard wall potential. This corresponds to the boundary condition that the induced polarization as a superposition of the bulk exciton states becomes zero at the surface. Therefore our calculations coincide with the results of the macroscopic theory with the Pekar type ABC. For the calculation of scattering spectrum alone, the macroscopic approach with an assumed form of the ABC is simpler than the reformulated nonlocal theory. However, the present procedure allows a detailed analysis in terms of the radiative shifts and widths, and the decomposition of the response field into the exciton and Mie scatterings.

Because of this advantage, we can discuss how the exciton scattering appears in the total cross section. In some cases a dip structure is found around the energy where the exciton scattering occurs. This can be seen when the Mie and exciton scatterings with J become comparable.

Another merit to adopt the present scheme is that we can calculate the energies of the exciton-light coupled modes. The real and imaginary parts of the energies correspond to the spectral peak energies and radiative widths of spectra, respectively. We have revealed the cavity effect on the radiative width. Namely, the radiative width of each peak shows a local maximum as a function of radius, at which the coupling becomes maximum. We have derived an analytic expression for this condition approximately.

Finally, we remark the extinction cross section and absorption spectra, which are observed experimentally much easier than the scattering cross section. The extinction and absorption spectra can be calculated in the microscopic nonlocal theory as is demonstrated in Appendix C. We confined ourselves to present numerical calculations of scattering cross section since we have the same results on the radiative peak shift and radiative widths for extinction and absorption spectra. This comes from the fact that these radiative corrections relate to the exciton-light interaction, which is independent of observation methods. It is noted that the dip structure in the scattering cross section does not appear in the extinction spectra because the extinction spectra are proportional to the real part of the coefficient of scattered field, i.e., there is no interference term of exciton and Mie scatterings.

ACKNOWLEDGMENTS

We would like to thank Professor H. Ishihara for useful discussions. This work was partly supported by a Grant-in-Aid for Encouragement of Young Scientists (13740186) and for COE Research (10CE2004) of the Ministry of Education, Science, Sports and Culture of Japan.

APPENDIX A: RELATIONSHIP OF DIFFERENT KINDS OF VECTOR FUNCTIONS

In this appendix, we present the relations of some vector functions used in this paper. First, we consider the relations between spherical vector function $\mathbf{Y}_{nJlM}$ and vector functions $\{\nabla\times\mathbf{r}z_l(kr)Y_{lm},\ \nabla\times\nabla\times\mathbf{r}z_l(kr)Y_{lm}\}$, where $z_l(kr)$ represents the spherical Bessel functions $j_l(kr)$ or $h_l^{(1)}(kr)$. The vector spherical harmonics relate to the spherical harmonics multiplied by the unit vector $\hat{\mathbf{r}}$ as follows:

$$\hat{\mathbf{r}}Y_{lm} = -\sqrt{\frac{l+1}{2l+1}}\mathbf{Y}_{l,l+1,m} + \sqrt{\frac{l}{2l+1}}\mathbf{Y}_{l,l-1,m}. \tag{A1}$$

Furthermore, we need the operations of curl to the types of $\{\Phi(r)\mathbf{Y}_{llm}, \Phi(r)\mathbf{Y}_{l,l\pm1,m}\}$ with $\Phi(r)$ being an arbitrary radial functions, and the results are given by

$$\boldsymbol{\nabla}\times[\Phi(r)\mathbf{Y}_{l,l+1,m}]=i\left(\frac{d}{dr}+\frac{l+2}{r}\right)\Phi\sqrt{\frac{l}{2l+1}}\mathbf{Y}_{llm}, \tag{A2}$$

$$\boldsymbol{\nabla}\times[\Phi(r)\mathbf{Y}_{llm}]=i\left(\frac{d}{dr}-\frac{l}{r}\right)\Phi\sqrt{\frac{l}{2l+1}}\mathbf{Y}_{l,l+1,m}+i\left(\frac{d}{dr}+\frac{l+1}{r}\right)\Phi\sqrt{\frac{l+1}{2l+1}}\mathbf{Y}_{l,l-1,m}, \tag{A3}$$

$$\boldsymbol{\nabla}\times[\Phi(r)\mathbf{Y}_{l,l-1,m}]=i\left(\frac{d}{dr}-\frac{l-1}{r}\right)\Phi\sqrt{\frac{l+1}{2l+1}}\mathbf{Y}_{llm}. \tag{A4}$$

After straightforward calculations using the above formulas, we get the relations

$$\boldsymbol{\nabla}\times[\mathbf{r}z_l(kr)Y_{lm}]=-i\sqrt{l(l+1)}z_l(kr)\mathbf{Y}_{llm}, \tag{A5}$$

$$\frac{1}{k}\boldsymbol{\nabla}\times\boldsymbol{\nabla}\times[\mathbf{r}z_l(kr)Y_{lm}]=\sqrt{\frac{l(l+1)}{2l+1}}\times[-\sqrt{l}z_{l+1}(kr)\mathbf{Y}_{l,l+1,m}+\sqrt{l+1}z_{l-1}(kr)\mathbf{Y}_{l,l-1,m}]. \tag{A6}$$

There exist another type of vector functions $\mathbf{M}_{oml}$ and $\mathbf{N}_{eml}$ defined in Eqs. (42) and (43). From the relation of the spherical harmonics and the associated Legendre function, we have

$$\mathbf{M}_{oml}=\alpha_{lm}\{\boldsymbol{\nabla}\times[\mathbf{r}z_l(kr)Y_{lm}]-\boldsymbol{\nabla}\times[\mathbf{r}z_l(kr)Y^*_{lm}]\}, \tag{A7}$$

$$\mathbf{N}_{eml}=i\alpha_{lm}\frac{1}{k}\{\boldsymbol{\nabla}\times\boldsymbol{\nabla}\times[\mathbf{r}z_l(kr)Y_{lm}]+\boldsymbol{\nabla}\times\boldsymbol{\nabla}\times[\mathbf{r}z_l(kr)Y^*_{lm}]\}, \tag{A8}$$

with

$$\alpha_{lm}=\frac{(-1)^m}{2i}\sqrt{\frac{4\pi}{2l+1}\frac{(l+m)!}{(l-m)!}}. \tag{A9}$$

Thus the vector functions $\{\mathbf{M}_{oml},\mathbf{N}_{eml}\}$ can be represented in terms of the vector spherical harmonics by using Eqs. (A5) and (A6).

Finally, we give the transformation of $\hat{\mathbf{r}}\hat{\mathbf{r}}'\,\delta(\mathbf{r}-\mathbf{r}')$, which appear in the last term of Eq. (24). The delta function can be expanded as

$$\delta(\mathbf{r}-\mathbf{r}')=\frac{1}{r^2}\delta(r-r')\,\delta(\Omega-\Omega')=\frac{1}{r^2}\delta(r-r')\sum_{lm}Y_{lm}(\Omega)Y^*_{lm}(\Omega'). \tag{A10}$$

If we use the relation in Eq. (A1), the dyadic function $\hat{\mathbf{r}}\hat{\mathbf{r}}'\,\delta(\mathbf{r}-\mathbf{r}')$ can be rewritten in terms of the vector spherical harmonics.

APPENDIX B: FORMULAS FOR INTEGRATION

We summarize the useful integral formulas for the calculations of Eqs. (34)–(38):

$$\int_0^x dx'x'^2 j_l(\alpha x')j_l(\beta x')=\begin{cases}\dfrac{x^2}{\alpha^2-\beta^2}[\alpha j_{l+1}(\alpha x)j_l(\beta x)-\beta j_l(\alpha x)j_{l+1}(\beta x)] & (\alpha\neq\beta)\\ \dfrac{x^2}{2\alpha}\{\alpha x[j_l^2(\alpha x)+j_{l+1}^2(\alpha x)] & \\ -(2l+1)j_l(\alpha x)j_{l+1}(\alpha x)\} & (\alpha=\beta)\end{cases}$$

and

$$\int_0^1 dx\int_0^1 dx'x^2x'^2 j_l(\alpha x)j_l(\beta x')j_l(\gamma x_<)h_l^{(1)}(\gamma x_>)=\begin{cases}\dfrac{\alpha j_{l+1}(\alpha)j_l(\gamma)-\gamma j_l(\alpha)j_{l+1}(\gamma)}{\alpha^2-\gamma^2} & \\ \times\dfrac{\beta j_{l+1}(\beta)h_l^{(1)}(\gamma)-\gamma j_l(\beta)h_{l+1}^{(1)}(\gamma)}{\beta^2-\gamma^2} & \\ -i\dfrac{\alpha j_{l+1}(\alpha)j_l(\beta)-\beta j_l(\alpha)j_{l+1}(\beta)}{\gamma(\alpha^2-\beta^2)(\beta^2-\gamma^2)} & (\alpha\neq\beta)\\ \dfrac{\alpha j_{l+1}(\alpha)j_l(\gamma)-\gamma j_l(\alpha)j_{l+1}(\gamma)}{\alpha^2-\gamma^2} & \\ \times\dfrac{\alpha j_{l+1}(\alpha)h_l^{(1)}(\gamma)-\gamma j_l(\alpha)h_{l+1}^{(1)}(\gamma)}{\alpha^2-\gamma^2} & \\ -i\dfrac{\alpha[j_l^2(\alpha)+j_{l+1}^2(\alpha)]-(2l+1)j_l(\alpha)j_{l+1}(\alpha)}{2\alpha\gamma(\alpha^2-\gamma^2)} & \\ (\alpha=\beta).\end{cases}$$

APPENDIX C: EXTINCTION AND ABSORPTION CROSS SECTIONS

The present approach using the microscopic nonlocal theory can provide the extinction and absorption cross sections also. Since the expression of the extinction cross section is given in Ref. 17 for Mie scattering, we focus on the contribution of exciton. In Ref. 17, the extinction cross section is represented in terms of the coefficients of the basis $\mathbf{M}_{oml}^{(3)}$ and $\mathbf{N}_{eml}^{(3)}$ for a scattered field, where $\mathbf{M}_{oml}^{(3)}$ and $\mathbf{N}_{eml}^{(3)}$ denote the vector functions defined by Eqs. (A7) and (A8) with $z_l(kr)=h_l^{(1)}(kr)$. Thus we obtain the extinction cross section due to exciton by changing the basis of scattered field

in Eqs. (51) and (52) from $\mathbf{Y}_{JlM}$ to $\mathbf{M}^{(3)}_{oml}$ and $\mathbf{N}^{(3)}_{eml}$ and comparing the results to the expression of extinction in Ref. 17. Note that the absorption cross section is given by subtracting the scattering cross section from the extinction cross section.

Using the transformations in Appendix A, we get the relations

$$\mathbf{M}^{(3)}_{o1l}=\sqrt{\pi}\frac{l(l+1)}{\sqrt{2l+1}}h^{(1)}_l(kr)(\mathbf{Y}_{ll1}+\mathbf{Y}_{ll,-1}), \tag{C1}$$

$$\mathbf{N}^{(3)}_{e1l}=\sqrt{\pi}\,\frac{l(l+1)}{2l+1}[\,\sqrt{l}h^{(1)}_{l+1}(kr)(\mathbf{Y}_{l,l+1,1}-\mathbf{Y}_{l,l+1,-1}) - \sqrt{l+1}h^{(1)}_{l-1}(kr)(\mathbf{Y}_{l,l-1,1}-\mathbf{Y}_{l,l-1,-1})], \tag{C2}$$

where we use the relation $\mathbf{Y}^*_{JlM}=(-1)^{J+M+l+1}\mathbf{Y}_{Jl,-M}$.

It is noted that M dependence of the constants U_{nJM} and V_{nJM} appears in F_{nJlM} determined from Eq. (9). The M-dependent elements in the equation are contained only in $F^{(0)}_{\xi}$ expressed in Eqs. (48)–(50), from which it is found that the value M determines just the sign of U_{nJM} and V_{nJM}. Then we have the relations

$$U_{nJ,-1}=U_{nJ1}, \quad V_{nJ,-1}=-V_{nJ1}. \tag{C3}$$

Therefore the sum of the $M=1$ and -1 components of $\mathbf{E}^{\mathrm{TE(TM)}}_{\mathrm{ex}}$ is proportional to the basis $\mathbf{M}_{o1l}$, $(\mathbf{N}_{e1l})$, and we get

$$\mathbf{E}^{\mathrm{TE}}_{\mathrm{ex}}=\frac{\eta k_1^3}{\sqrt{\pi}}\frac{\mu}{\epsilon_1}\sum_{nJ}\frac{\sqrt{2J+1}}{J(J+1)}U_{nJ1}\mathbf{M}^{(3)}_{o1J}, \tag{C4}$$

$$\mathbf{E}^{\mathrm{TM}}_{\mathrm{ex}}=\frac{\eta k_1^3}{\sqrt{\pi}}\frac{\mu}{\epsilon_1}\sum_{nJ}\frac{2J+1}{J(J+1)}V_{nJ1}\mathbf{N}^{(3)}_{e1J}. \tag{C5}$$

From the expansion coefficients of $\mathbf{M}^{(3)}_{o1J}$ and $\mathbf{N}^{(3)}_{e1J}$, we have the extinction cross sections by exciton $\overline{\sigma^{\mathrm{TE(TM)}}_{\mathrm{ex}}}$ as follows:

$$\overline{\sigma^{\mathrm{TM}}_{\mathrm{ex}}}=\frac{4\sqrt{2}\pi}{E_i}\frac{\sqrt{\epsilon_1}}{\epsilon_2}\kappa_1\sqrt{\Delta_{LT}a}\sum_{nJ}\sqrt{2J+1}\mathrm{Re}[(-i)^{J+1}U_{nJ1}]. \tag{C6}$$

$$\overline{\sigma^{\mathrm{TE}}_{\mathrm{ex}}}=\frac{4\sqrt{2}\pi}{E_i}\frac{\sqrt{\epsilon_1}}{\epsilon_2}\kappa_1\sqrt{\Delta_{LT}a}\sum_{nJ}(2J+1)\mathrm{Re}[(-i)^{J}V_{nJ1}], \tag{C7}$$

[1] H. Ajiki and K. Cho, in *Proceedings of the 3rd International Conference on Excitonic Processes in Condensed Matter, Boston, 1998*, edited by R. T. Willians and W. M. Yen (Electrochemical Society, Pennington, NJ, 1999) p. 262.
[2] H. Ajiki and K. Cho, Phys. Rev. B **62**, 7402 (2000).
[3] A. Ekimov, A. Onushchenko, M. Raikh, and A. L. Efros, Sov. Phys. JETP **63**, 1054 (1986).
[4] R. Ruppin, J. Phys. Chem. Solids **50**, 877 (1989).
[5] S. Pekar, Sov. Phys. JETP **6**, 785 (1958).
[6] K. Cho, Prog. Theor. Phys. Suppl. **106**, 225 (1991).
[7] G. Mie, Ann. Phys. (N.Y.) **25**, 377 (1908).
[8] K. Cho, J. Phys. Soc. Jpn. **68**, 683 (1999).
[9] H. Ishihara and K. Cho, Phys. Rev. B **48**, 7960 (1993).
[10] K. Cho and J. Ushida, in *Elementary Processes in Excitations and Reactions on Solid Surfaces*, edited by A. Okiji, H. Kasai, and K. Makoshi (Springer, Berlin, 1996), p. 193.
[11] W. Chew, *Waves and Fields in Inhomogeneous Media* (IEEE press, Piscataway, NJ, 1995).
[12] A. D'Andrea and R. DelSole, Phys. Rev. B **25**, 3714 (1982).
[13] W. Heller and A. Marcus, Phys. Rev. **84**, 809 (1951).
[14] Y. Onodera and Y. Toyozawa, J. Phys. Soc. Jpn. **22**, 833 (1967).
[15] K. Cho, in *Proceedings of the 14th International Conference on Physics of Semiconductors, Bristol and London*, 1978, edited by B.L.H. Wilson (IOP, Bristol, 1979) p. 841.
[16] A. Edmonds, *Angular Momentum in Quantum Mechanics* (Princeton University Press, Princeton, NJ, 1996).
[17] C. Bohren and D. Huffman, *Absorption and Scattering of Light by Small Particles* (Wiley, New York, 1983).
[18] T. Mita and N. Nagasawa, Solid State Commun. **44**, 1003 (1982).
[19] K. Cho, J. Phys. Soc. Jpn. **66**, 2496 (1997).
[20] H. Ishihara, H. Asakawa, and K. Cho, Physica E **7**, 671 (2000).
[21] H. Ishihara, Physica E (to be published).
[22] H. Ajiki, J. Lumin. **94-95**, 173 (2001).